RSC Advances

PAPER

View Article Online
View Journal | View Issue

Cite this: *RSC Adv.*, 2018, **8**, 8199

The effect of 3D carbon nanoadditives on lithium hydroxide monohydrate based composite materials for highly efficient low temperature thermochemical heat storage

Shijie Li,[ab] Hongyu Huang,[*a] Jun Li,[*c] Noriyuki Kobayashi,[c] Yugo Osaka,[d] Zhaohong He[a] and Haoran Yuan[a]

Lithium hydroxide monohydrate based thermochemical heat storage materials were modified with *in situ* formed 3D-nickel-carbon nanotubes (Ni-CNTs). The nanoscale (5–15 nm) $LiOH \cdot H_2O$ particles were well dispersed in the composite formed with Ni-CNTs. These composite materials exhibited improved heat storage capacity, thermal conductivity, and hydration rate owing to hydrogen bonding between H_2O and hydrophilic groups on the surface of Ni-CNTs, as concluded from combined results of *in situ* DRIFT spectroscopy and heat storage performance test. The introduction of 3D-carbon nanomaterials leads to a considerable decrease in the activation energy for the thermochemical reaction process. This phenomenon is probably due to Ni-CNTs providing an efficient hydrophilic reaction interface and exhibiting a surface effect on the hydration reaction. Among the thermochemical materials, Ni-CNTs–$LiOH \cdot H_2O$-1 showed the lowest activation energy (23.3 kJ mol^{-1}), the highest thermal conductivity (3.78 W m^{-1} K^{-1}) and the highest heat storage density (3935 kJ kg^{-1}), which is 5.9 times higher than that of pure lithium hydroxide after the same hydration time. The heat storage density and the thermal conductivity of Ni-CNTs–$LiOH \cdot H_2O$ are much higher than 1D MWCNTs and 2D graphene oxide modified $LiOH \cdot H_2O$. The selection of 3D carbon nanoadditives that formed part of the chemical heat storage materials is a very efficient way to enhance comprehensive performance of heat storage activity components.

Received 10th January 2018
Accepted 16th February 2018

DOI: 10.1039/c8ra00269j

rsc.li/rsc-advances

1. Introduction

As an important part of clean and efficient utilization of alternative energy, the development of thermal energy storage technology has become increasingly important in recent years owing to the incremental consumption of fossil energy and the emission of greenhouse gases.[1,2] These technologies are divided into three main types: sensible heat storage,[3,4] latent heat storage,[5,6] and thermochemical heat storage.[7,8] All of these technologies participate in solving the supply and demand mismatch of thermal energy, and improve energy efficiency.[9] Among these technologies, thermochemical heat storage, which uses reversible chemical reactions to store and release thermal energy, facilitates the efficient utilization of thermal energy due to its high heat storage density.[10] Based on heat storage working temperature, the thermochemical heat storage technology could be divided into two parts: high temperature heat storage and low temperature heat storage.[9,10] As core components of these technologies, numerous thermochemical materials (TCMs) have been selected. For instance, metal hydroxides, metal hydrides, and metal carbonates are typically used as TCMs for high-temperature thermochemical heat storage, whereas inorganic salt hydrates and salt ammoniate are considered as promising candidates for low-temperature thermochemical heat storage due to their different decomposition temperature.[11–16] For efficiently storing low-temperature thermal energy, the inorganic hydrate lithium hydroxide monohydrate ($LiOH \cdot H_2O$), which possesses high energy density (1440 kJ kg^{-1}) and mild reaction process, was selected as a potential material.[17] However, similar to other inorganic hydrates[18,19] pure $LiOH \cdot H_2O$ exhibit low hydration rate and thermal conductivity;[15,17] moreover, its heat storage density decreases after hydration, thereby seriously limiting the application of the material. Hence, composite TCMs with high heat

[a]*Key Laboratory of Renewable Energy, Guangdong Provincial Key Laboratory of New and Renewable Energy Research and Development, Guangzhou Institute of Energy Conversion, Chinese Academy of Sciences, No. 2 Nengyuan Rd, Wushan, Tianhe District, Guangzhou 510640, P. R. China. E-mail: lisj@ms.giec.ac.cn; huanghy@ms.giec.ac.cn; hezh@ms.giec.ac.cn; yuanhr@ms.giec.ac.cn*

[b]*University of Chinese Academy of Sciences, Beijing 100049, PR China*

[c]*Nagoya University, Furo-cho, Chikusa-ku, Nagoya-shi, Aichi 464-8603, Japan. E-mail: Junli@energy.gr.jp; kobayashi@energy.gr.jp*

[d]*Kanazawa University, Kanazawa-shi, Ishikawa-ken 920-1192, Japan. E-mail: y-osaka@se.kanazawa-u.ac.jp*

storage density and high thermal conductivity are of considerable synthetic value.

3D carbon nanomaterials (3D-carbon nanotube sponge and arrays[20,21]), which exhibit large surface area, low bulk density, and chemical stability,[22–24] are widely used in various fields, such as electronics[25,26] and catalysis[24,27] as typical carbon nanomaterials. In addition, these materials offer excellent hydrophilic property after the introduction of surface oxygen groups. However, under normal conditions, traditional one-dimensional or two-dimensional carbon nanomaterials are selected and used for latent heat thermal energy storage.[2,28,29] 3D carbon nanomaterials are rarely used for thermal energy storage,[30] especially thermochemical heat storage. In our previous work, 1D carbon nanomaterials,[31] MWCNTs were used to modify $LiOH \cdot H_2O$; heat storage performance was markedly enhanced, but the thermal conductivity needed improvement. Hence, 2D-carbon nanomaterial[15,32] graphene oxide was selected and, which markedly improved the energy storage performance of $LiOH \cdot H_2O$ and $Mg(OH)_2$. Graphene oxide also positively affected thermal conductivity to a certain extent. Hydrophilic substances, such as lithium chloride (LiCl), 13X-zeolite, and NaY-zeolite, were also used to enhance the heat storage performance and obtain expected results.[33] Kato *et al.* investigated the reaction behavior of metal-salt modified $Mg(OH)_2$-based materials; during the heat storage process, LiCl and LiBr acted as catalysts and decreased the activation energy effectively and substantially improved heat storage performance.[5,11,34] Moreover, the functional groups on the surface of the materials markedly affected the reaction behavior of $Mg(OH)_2$. However, the relationship between heat storage density and particle size, especially when materials reached nanoscale, was not discussed. In this work, *in situ* DRIFT spectroscopy technology and chemical reaction kinetics test were used for an in-depth analysis of the heat storage mechanism, which has not been involved in previous research. Moreover, to simultaneously improve the performance of heat storage density, hydration rate, and thermal conductivity, we synthesized a novel TCM composite of *in situ* formed 3D-nickel-carbon nanotubes (Ni-CNTs) and $LiOH \cdot H_2O$. Four kinds of TCMs were prepared, and the effect of 3D-carbon nanomaterials was extensively investigated. The highest heat storage density of Ni-CNTs–$LiOH \cdot H_2O$ could reach 3935 kJ kg^{-1}, which is 2.2 times higher than that of 1D MWCNTs modified $LiOH \cdot H_2O$ (1804 kJ kg^{-1}) and the thermal conductivity (3.78 W m^{-1} K^{-1}) is also much higher than MWCNTs modified $LiOH \cdot H_2O$ (1.75 W m^{-1} K^{-1})[31] The heat storage density and the thermal conductivity of Ni-CNTs modified $LiOH \cdot H_2O$ are also higher than 2D graphene oxide modified $LiOH \cdot H_2O$ (1980 kJ kg^{-1}; 1.70 W m^{-1} K^{-1}), respectively.[15] It indicated that the selection of 3D nano carbon materials as composed part of the chemical heat storage materials is a very efficient way to enhance comprehensive performance of heat storage activity component.

2. Experimental

2.1. Raw materials and synthesis method of $LiOH \cdot H_2O$-based TCMs

The 3D-carbon nanotubes were synthesized by catalytic chemical vapor deposition method with C_2H_4 as carbon source and nickel foam as catalyst.[35] First, nickel foam was placed in a tubular furnace, which was heated to 700 °C, and filled with Ar/H_2 (300 mL/100 mL) mixed reducing gas for 2 h. After reduction, Ar/H_2 mixed gas was replaced with Ar/C_2H_4 (400 mL/100 mL), the temperature was increased to 550 °C, and the system was allowed to react for 20 min. After the temperature decreased to 25 °C, the 3D Ni skeleton CNTs (Ni-CNTs) was obtained. Then, after being oxidized by 5% O_2 for 2 h at 250 °C, the as-prepared 3D Ni-CNTs were composited with $LiOH \cdot H_2O$ by impregnation method. First, 0.5 g $LiOH \cdot H_2O$ was dissolved in 1 mL deionized water under vigorous stirring. Subsequently, 3D nanocarbon were added in the LiOH aqueous solution at room temperature, and the mixture was stirred continuously for 4 h. Afterward, the products were withdrawn and vacuum freeze-dried. The obtained materials with different $LiOH \cdot H_2O$ content (14 wt%, 23 wt%, 39 wt%, 100 wt%) were named as Ni-CNTs–$LiOH \cdot H_2O$-1, Ni-CNTs–$LiOH \cdot H_2O$-2, Ni-CNTs–$LiOH \cdot H_2O$-3, and $LiOH \cdot H_2O$, respectively.

2.2. The characterization and heat storage performance test method of $LiOH \cdot H_2O$-based TCMs

Surface topography was measured by field-emission scanning electron microscopy (SEM, S-4800, Hitachi Limited). Transmission electron micrographs (TEM) were obtained with FEI Tecnai G212 operated at 100 kV and a JEOL JEM-2100F operated at 200 kV. X-ray diffraction (XRD) analysis was performed on a D8-advance X-ray diffractometer (Bruker, Germany) with Cu target (40 kV, 40 mA). The scan step size was 0.0167°, and counting time was 10.160 s. Nitrogen adsorption–desorption was measured at the boiling point of nitrogen (77 K) by a Quantachrome QDS-30 analyzer. BET (Brunauer–Emmett–Teller) surface area and pore structure were measured by nitrogen physisorption under normal relative pressure of 0.1–1.0. The thermal conductivity of the sample was measured by a DRL-II thermal conductivity tester (Xiangtan Xiangyi Instrument Co., Ltd.). $LiOH \cdot H_2O$, Ni-CNTs–$LiOH \cdot H_2O$-1, Ni-CNTs–$LiOH \cdot H_2O$-2, Ni-CNTs–$LiOH \cdot H_2O$-3 were used as raw substance then, LiOH Ni-CNTs–LiOH-1, Ni-CNTs–LiOH-2, and Ni-CNTs–LiOH-3 were synthesized by decomposing $LiOH \cdot H_2O$, Ni-CNTs–$LiOH \cdot H_2O$-1, Ni-CNTs–$LiOH \cdot H_2O$-2, and Ni-CNTs–$LiOH \cdot H_2O$-3 in a horizontal tubular quartz furnace with Ar gas at 150 °C for 3 h. Dehydrated products were cooled to 30 °C in an Ar atmosphere, and water vapor at a partial pressure of 2.97 kPa and carried by N_2 flow was introduced to the tube for 60 min for hydration operation at 30 °C. After hydration, the endothermic heat and temperature of the samples were measured through Thermogravimetry and Differential Scanning Calorimetry (TG-DSC) (STA-200, Nanjingdazhan Co., Ltd.), which was also used for measuring weight change during dehydration step. Each TG-DSC measurement was repeated three times in order to ensure correctness. The activation energy of dehydration performance of all samples was calculated using Ozawa method,[36] which is applicable for calculating the activation energy of thermal decomposition and dehydration reaction. By using the Ozawa method, the following equation can be obtained based on the reaction rate expression and the Arrhenius's equation:

$$\ln\left(\frac{\beta}{T^2}\right) = \ln\frac{R}{E}\frac{A}{f(\alpha)} - \frac{E}{R}\frac{1}{T}$$

In this equation, E is the activation energy (kJ mol^{-1}), β is the heating rate (K s^{-1}), T is temperature (K), R is the ideal gas constant (J (mol K)$^{-1}$), A is a pre-exponential factor, α is the dehydration conversion, and $f(\alpha)$ is a function of dehydration conversion. During the calculation of activation energy, the dehydration conversion was maintained at 70%. The heating rates were 3 K min^{-1}, 7 K min^{-1} and 10 K min^{-1}, and the activation energy was obtained from the slope ($-E/R$) of this equation.

3. Results and discussion

3.1. Microstructure characterization of LiOH·H$_2$O-based TCMs

Fig. 1 shows the XRD patterns of LiOH·H$_2$O, Ni-CNTs–LiOH·H$_2$O-1, Ni-CNTs–LiOH·H$_2$O-2, and Ni-CNTs–LiOH·H$_2$O-3 samples. As shown in Fig. 1, the diffraction peaks at around 30°, 32.19°, 33.64°, 34.84°, 37.07°, 38.83°, 40.06°, 41.61°, 43.49°, 49.37°, 51.36°, 52.47°, 55.15°, 55.70°, 56.92°, 62.15°, 63.13°, 64.55°, 65.47°, 66.22°, 68.35° and 71.34°, respectively, were attributed to LiOH·H$_2$O, whereas the diffraction peaks at around 25° were attributed to graphitic carbon.[37] Meanwhile, the diffraction peaks at around 45°, 52°, and 77° could be assigned to metal nickel. It could be clearly seen that the diffraction peaks of LiOH·H$_2$O were sharp and strong in the LiOH·H$_2$O sample, but the diffraction peaks of LiOH·H$_2$O became weaker and more diffused when 3D carbon nanomaterial Ni-CNTs were added. Hence, the composites of Ni-CNTs and LiOH·H$_2$O were successfully synthesized, and the addition of Ni-CNTs resulted in the extensive dispersion of LiOH·H$_2$O particles in the composite materials.

Fig. 2a–d provide the SEM images of LiOH·H$_2$O, Ni-CNTs–LiOH·H$_2$O-1, Ni-CNTs–LiOH·H$_2$O-2, and Ni-CNTs–LiOH·H$_2$O-3, respectively. As shown in Fig. 2a, before the addition of 3D-carbon nanoadditives, the bulk LiOH·H$_2$O was aggregated with a large diameter (300 nm to 2 μm). After the modification of Ni-CNTs, no obvious change was observed in the regular structure for Ni-CNTs–LiOH·H$_2$O-1 (Fig. 2b) and Ni-CNTs–LiOH·H$_2$O-2 (Fig. 2c). This finding indicates that the intervention of LiOH·H$_2$O did not lead to structural deterioration at a mass ratio < 23% and that LiOH·H$_2$O was highly dispersed in the composite materials. This result agrees well with the XRD result. When the content of LiOH·H$_2$O reached 39% (Ni-CNTs–LiOH·H$_2$O-3), several LiOH·H$_2$O particles could be seen on the surface of Ni-CNTs (Fig. 2d).

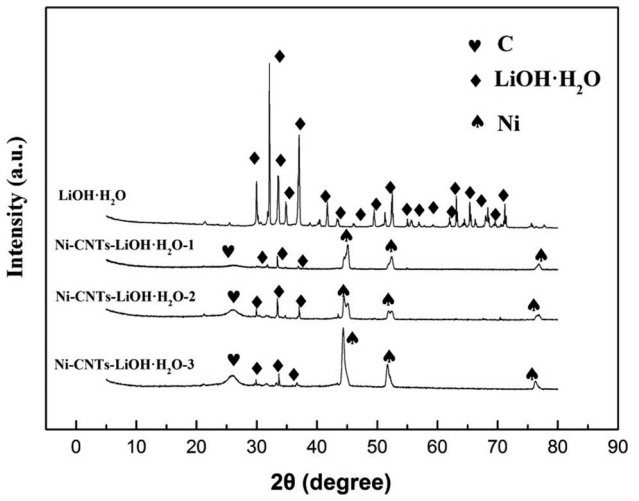

Fig. 1 XRD patterns of LiOH·H$_2$O, Ni-CNTs–LiOH·H$_2$O-1, Ni-CNTs–LiOH·H$_2$O-2, Ni-CNTs–LiOH·H$_2$O-3.

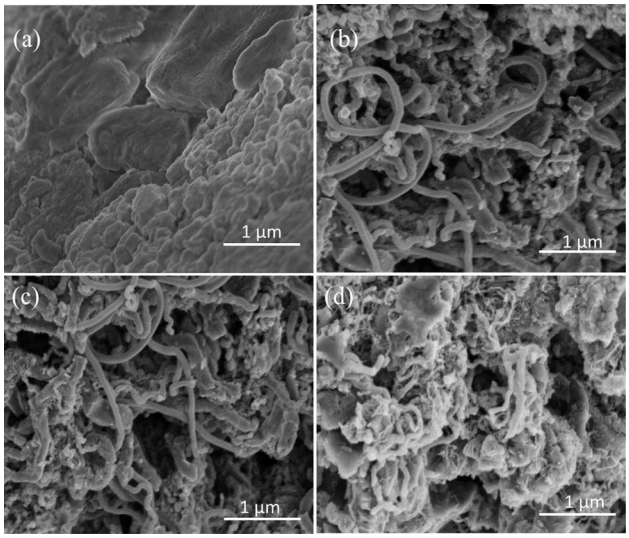

Fig. 2 SEM images of (a) LiOH·H$_2$O, (b) Ni-CNTs–LiOH·H$_2$O-1, (c) Ni-CNTs–LiOH·H$_2$O-2 and (d) Ni-CNTs–LiOH·H$_2$O-3.

Fig. 3 shows the TEM images of Ni-CNTs–LiOH·H$_2$O with different contents of LiOH·H$_2$O. In Fig. 3, LiOH·H$_2$O nanoparticles with a diameter around 5 nm were successfully dispersed on Ni-CNTs (Fig. 3b) with clear particle structure. LiOH·H$_2$O particle size showed a growth trend with increasing LiOH·H$_2$O content in Ni-CNTs–LiOH·H$_2$O composite materials (Fig. 3d and f). When LiOH·H$_2$O content reached 39% (Fig. 3f), the LiOH·H$_2$O nanoparticle size could increase to 15 nm, which is a bit bigger than the other two composite materials. Pure LiOH·H$_2$O (Fig. 2a) existed in the form of stacked flakes and showed the largest particle size (300 nm to 2 μm). The addition of Ni-CNTs can effectively induce nanoscale LiOH·H$_2$O dispersion, and the resulting particle size is markedly smaller than that of pure LiOH·H$_2$O. During the synthesis of Ni-CNTs–LiOH·H$_2$O composite materials, intermolecular interaction, such as hydrogen bonding, may exist between Ni-CNTs and LiOH·H$_2$O owing to the presence of oxygen-containing functional groups, such as hydroxyl, carbonyl, and carboxyl groups,[38–40] on the surface of Ni-CNTs. Therefore, proper additives supplied hydrogen bonding could show good ability for retarding the aggregation of LiOH·H$_2$O. The porosity structures of LiOH·H$_2$O were also measured by nitrogen adsorption–desorption. The BET specific surface area, pore volume, and average pore size are shown in Table 1. Ni-CNTs–LiOH·H$_2$O

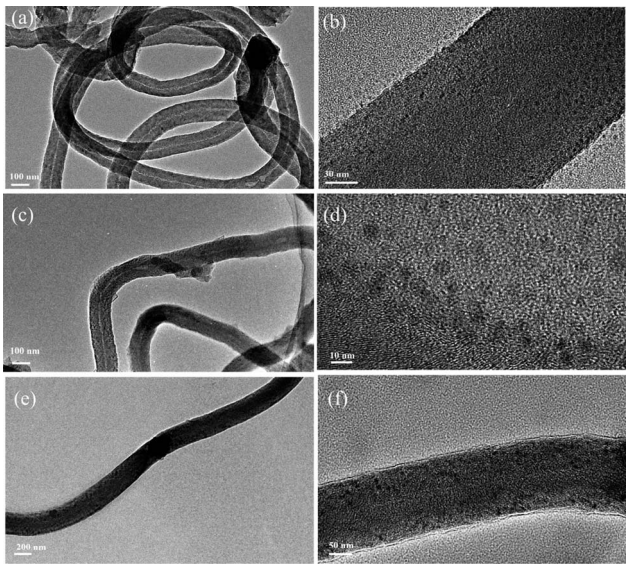

Fig. 3 TEM images of (a) Ni-CNTs–LiOH·H_2O-1, (c) Ni-CNTs–LiOH·H_2O-2, (e) Ni-CNTs–LiOH·H_2O-3, and HRTEM images of (b) Ni-CNTs–LiOH·H_2O-1 (d) Ni-CNTs–LiOH·H_2O-2 and (f) Ni-CNTs–LiOH·H_2O-3.

samples show different textures. Owing to the addition of Ni-CNTs with different mass ratio, Ni-CNTs–LiOH·H_2O shows a larger specific surface area than pure LiOH·H_2O (15 m^2 g^{-1}). According to SEM and TEM characterization results, high specific surface area is an important cause of the nanoscale dispersion of LiOH·H_2O particles.

3.2. Heat storage performance test on LiOH·H_2O-based TCMs

The heat storage performance test of pure LiOH·H_2O, Ni-CNTs–LiOH·H_2O-1, Ni-CNTs–LiOH·H_2O-2 and Ni-CNTs–LiOH·H_2O-3 were carried out and shown in Fig. 4. The *Y* axis is the amount of heating per unit time and mass (W g^{-1}), and the *X* axis is temperature. The area of the curve is proportional to the change of enthalpy, as for heat storage materials it stands for the heat storage density. The pure LiOH·H_2O heat storage density was only approximately 661 kJ kg^{-1} due to the slow reaction rate of LiOH and water vapor. In the hydration reaction, only about 42% of LiOH can be converted to LiOH·H_2O after 1 h of hydration, as calculated by approximately 18% mass loss of H_2O shown in Fig. 4a. By contrast Fig. 4b shows the DSC curve of 3D-carbon nanomaterial modified LiOH·H_2O. After 1 h of hydration of the Ni-CNTs–LiOH·H_2O composite, LiOH was fully hydrated to LiOH·H_2O, and the heat storage density of Ni-CNTs–LiOH·H_2O-1 normalized by LiOH·H_2O content can reach 3935 kJ kg^{-1}. High heat storage densities of 3505 kJ kg^{-1} and 2782 kJ kg^{-1} were observed in LiOH·H_2O contained in Ni-CNTs–LiOH·H_2O-2 (Fig. 4c) and Ni-CNTs–LiOH·H_2O-3 (Fig. 4d), respectively. Therefore, compared with pure LiOH and with the same duration of the hydration reaction LiOH, and H_2O molecule can be fully converted to LiOH·H_2O owing to the introduction of Ni-CNTs, the hydration reaction rate of Ni-CNTs–LiOH·H_2O was substantially improved. On the one hand, owing to the formation of hydrophilic functional groups on the surface of Ni-CNTs during preparation, H_2O adsorption became easier and provided a completely different reaction interface between LiOH and water molecules. On the other hand, Ni-CNTs–LiOH·H_2O showed ultrahigh heat storage density exceeding that of pure LiOH·H_2O owing to the existence of hydrophilic functional groups[41] and increased specific surface area, which markedly enhanced the dispersion of LiOH·H_2O nanoparticles and the contact surface area with water molecules. The low specific surface area of pure LiOH·H_2O may exert a negative effect on heat storage density. When the particle size reached nanoscale, the amount of surface atoms evidently increases; moreover, the crystalline field and binding energy of internal atoms were notably different from those of surface atoms, which possessed numerous dangling bonds owing to the lack of adjacent atoms. Hence, the unsaturated bonds in atoms show that nanoparticles present enhanced thermodynamic property.[42,43] Meanwhile, due to increased number of surface atoms and the existence of hydrophilic functional groups, more H_2O and LiOH can react, and therefore, heat storage performance can be improved. Furthermore, according to SEM and TEM characterization results, the heat storage density of Ni-CNTs–LiOH·H_2O was higher than that of LiOH·H_2O possible because of the smaller particle size of LiOH·H_2O (5–15 nm) in Ni-CNTs–LiOH·H_2O than that in pure LiOH·H_2O (300 nm to 2 μm). Thus, small-sized nanoparticles can notably contribute to the enhancement of heat storage density for composite materials; as the particle size expands, the heat storage density of LiOH·H_2O decreases. Furthermore, after the addition of Ni-CNTs to LiOH·H_2O, the thermal conductivity of composite materials evidently increased and exceeded that of pure LiOH·H_2O (Fig. 5) owing to the high thermal conductivity of Ni-CNTs. The highest thermal conductivity of Ni-CNTs–LiOH·H_2O can reach 3.78 W m^{-1} K^{-1}, which is 2.2 times higher than that of pure LiOH·H_2O.

Table 1 Texture parameters of carbon nanoadditives modified composed thermochemical materials and pure LiOH·H_2O

Samples	Surface area (m^2 g^{-1})	Pore volume (mL g^{-1})	Average pore size (nm)
Ni-CNTs	146	0.30	8.17
Ni-CNTs–LiOH·H_2O-1	119	0.20	6.79
Ni-CNTs–LiOH·H_2O-2	99	0.11	6.76
Ni-CNTs–LiOH·H_2O-3	62	0.14	5.62
Pure LiOH·H_2O	15	0.06	1.75

In situ DRIFT test was conducted to investigate the effect of hydrophilic functional groups of 3D-carbon nanotubes on the hydration/dehydration reaction of LiOH·H_2O. Raw materials LiOH·H_2O and the Ni-CNTs–LiOH·H_2O composite were exposed to a flow of N_2 (300 mL min^{-1}) at 150 °C to decompose for 24 h. Then, the as-prepared samples LiOH and Ni-CNTs–LiOH were placed in the *in situ* reactor of an FT-IR spectrometer. The reactor was vacuumed and purged using a He flow. The *in situ* DRIFT test started with the hydration reaction of LiOH and H_2O and finished with dehydration reaction of LiOH·H_2O.

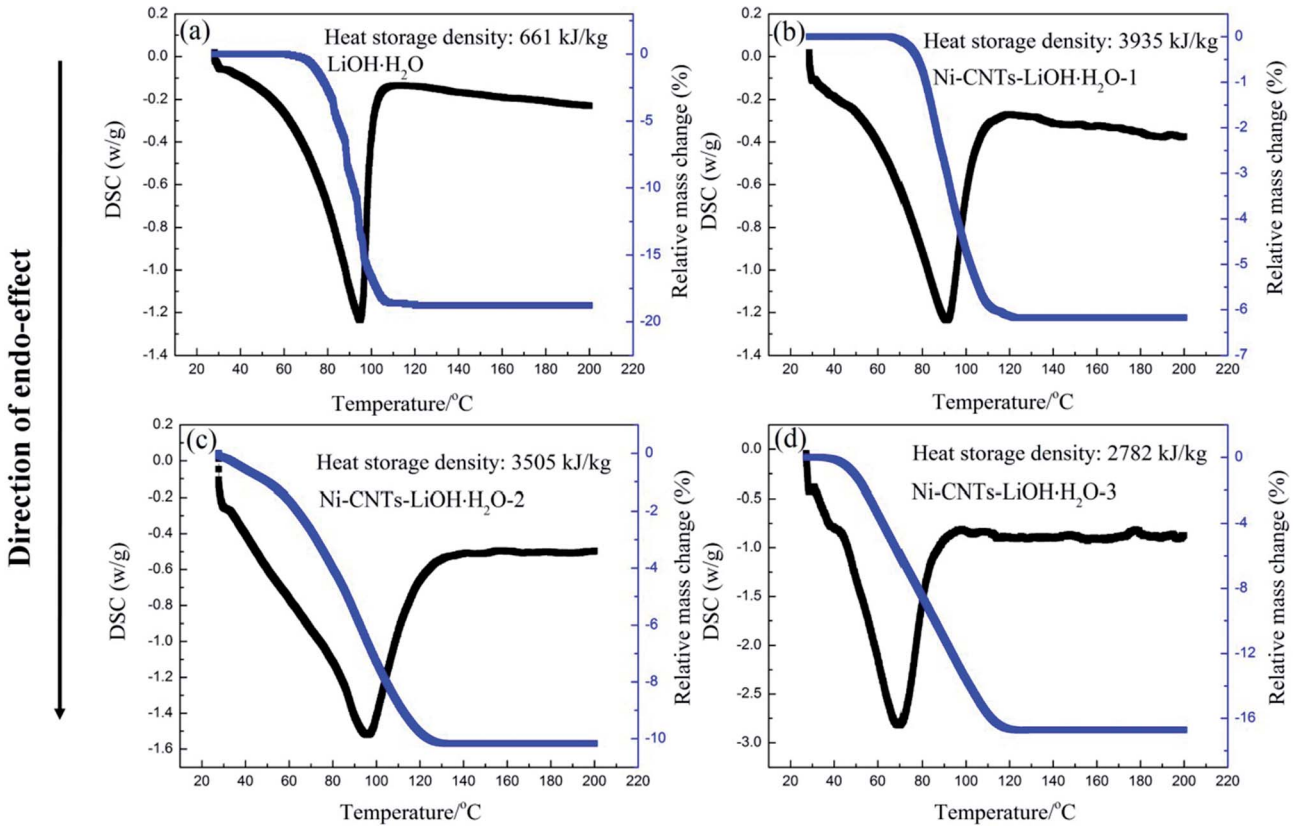

Fig. 4 TG-DSC curves of as-synthesized samples: (a) pure LiOH after 1 h hydration, (b) Ni-CNTs–LiOH-1 after 1 h hydration, (c) Ni-CNTs–LiOH-2 after 1 h hydration, and (d) Ni-CNTs–LiOH-3 after 1 h hydration.

Fig. 6a shows the *in situ* DRIFT spectroscopy of the hydration reaction of LiOH and H_2O. The bands in the range of 3800–2200 cm^{-1} are always assigned to the stretching vibrations of structural OH groups and physical adsorbed H_2O molecules.[44] In the spectra, the peak at around 3679 cm^{-1} and 1573 cm^{-1} could be attributed to the stretching vibrations (ν_{OH}) and bending vibrations (β_{OH}) of the structure water in LiOH·H_2O, respectively.[45] Besides, broad peaks in the 2842–3423 cm^{-1} range were centered at around 3235 cm^{-1}. This peak (3235 cm^{-1}) and another peak at the lower band (1644 cm^{-1}) were the ν_{OH} and β_{OH} of OH, respectively, in the physical adsorbed H_2O.[44,46] In Fig. 6a it could be also observed that when the hydration reaction was ready for start, the weak peaks, which stand for OH in structure H_2O and physical adsorbed H_2O molecules have been existed. This finding may be due to the reaction of LiOH and residual physical adsorbed H_2O on the surface of LiOH. With prolonged hydration reaction, the peak intensities of structural OH (3679 cm^{-1} and 1573 cm^{-1}) markedly increased at 15 min hydration. These peaks slowly increased during 15 min to 120 min hydration reaction, indicating the continuous reaction of LiOH and water steam and the decrease in hydration reaction rate. During this reaction, no obvious change could be observed for the peak intensities of OH (3235 cm^{-1} and 1644 cm^{-1}) in physical adsorbed H_2O because of the steady water steam flow in the *in situ* reactor. After the hydration reaction, the reactor was vacuumed and purged using a dry He flow, then LiOH·H_2O was heated at a rate of 0.5 °C s^{-1} under the control of temperature-programmed technology.

Fig. 6b shows the *in situ* DRIFT spectroscopy of dehydration reaction of LiOH·H_2O obtained from 1 h hydration of LiOH. When LiOH·H_2O was heated to 60 °C, the peak intensities of OH in structural H_2O (3679 cm^{-1} and 1573 cm^{-1}) started to decrease. When the temperature exceeded 70 °C, the trend became more evident. Meanwhile, the peaks of OH (3235 cm^{-1} and 1644 cm^{-1}) in physical adsorbed H_2O appeared and increased from 60 °C to 80 °C, indicating the form of free water. The intensity of the peaks gradually decreased owing to easy

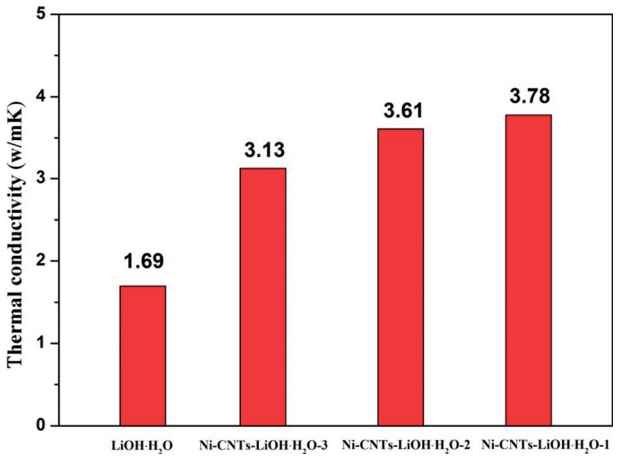

Fig. 5 Thermal conductivity of LiOH·H_2O, Ni-CNTs–LiOH·H_2O-1, Ni-CNTs–LiOH·H_2O-2 and Ni-CNTs–LiOH·H_2O-3.

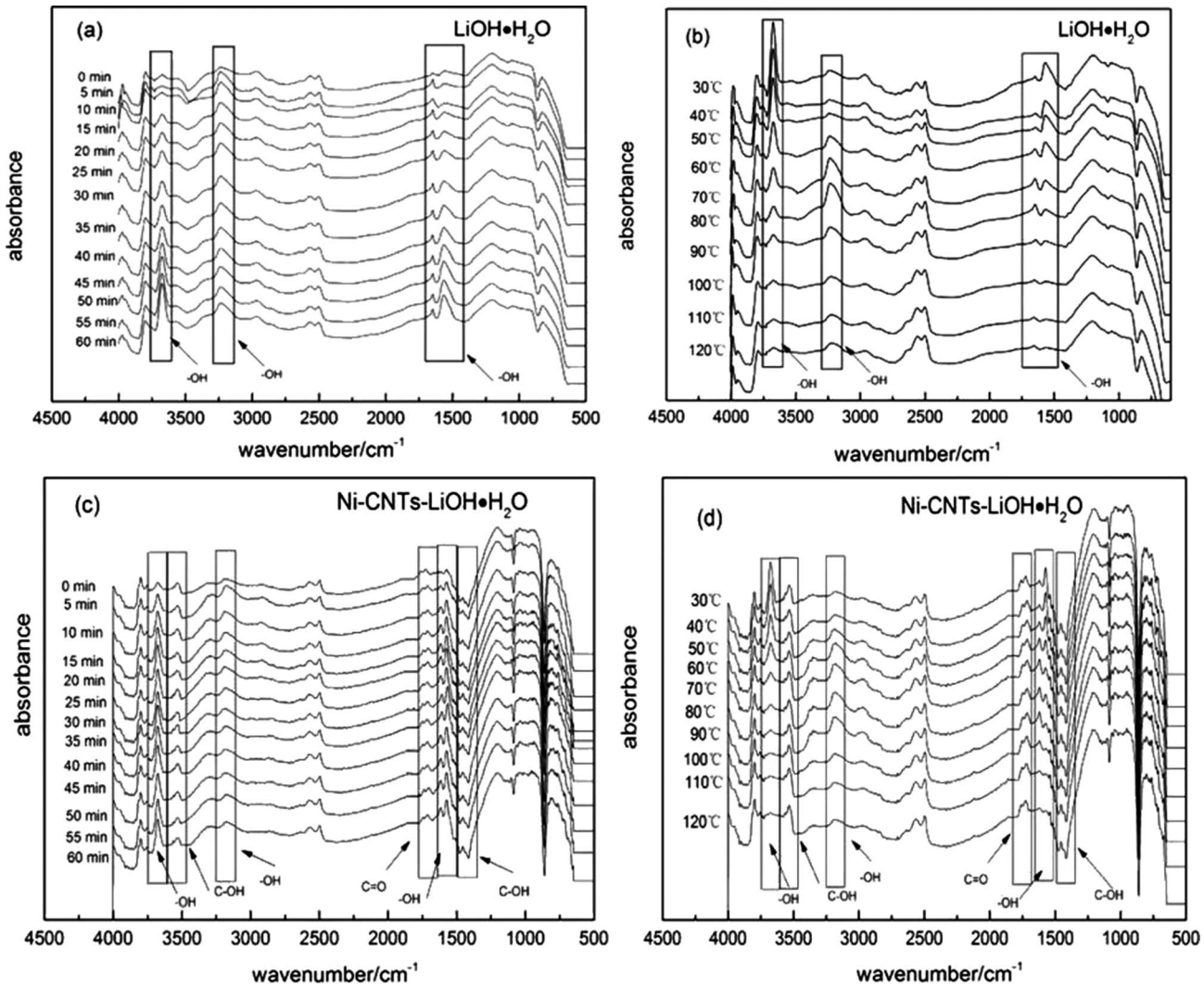

Fig. 6 (a) The *in situ* DRIFT spectroscopy of the hydration reaction of LiOH; (b) the *in situ* DRIFT spectroscopy of dehydration reaction of $LiOH \cdot H_2O$; (c) the *in situ* DRIFT spectroscopy of hydration reaction of Ni-CNTs–LiOH; (d) the *in situ* DRIFT spectroscopy of dehydration reaction of Ni-CNTs–$LiOH \cdot H_2O$.

desorption and blowing away of physical adsorbed water at elevated temperature.

Fig. 6c shows the *in situ* DRIFT spectroscopy of hydration reaction of Ni-CNTs–LiOH and H_2O. During hydration reaction, the peak intensities of OH in structure H_2O (3679 cm^{-1} and 1573 cm^{-1}) showed a marked increase with 5 min hydration because of the existing hydrophilic groups, such as C–OH and C=O, on the surface of 3D-carbon nanotubes. After 20 min, the peaks were virtually unchanged, which indicating that the hydration reaction rate of LiOH and water steam was enhanced, exceeding that of pure LiOH. The peak intensities of OH (3181 cm^{-1} and 1625 cm^{-1}) in physical adsorbed H_2O did not notably change. The band at around 3520 cm^{-1} can be assigned to stretching vibrations, whereas the band at around 1400 cm^{-1} was attributed to the bending vibrations of C–OH.[44] The band at 1720 cm^{-1} was assigned to C=O groups. When the water steam flowed into the reactor, the wavenumber of C=O groups shifted from 1720 cm^{-1} to 1710 cm^{-1} because of the formation of hydrogen bonding[2] between C=O groups and adsorbed H_2O. Owing to the effect of hydrogen bonding, the adsorption of H_2O on the surface of Ni-CNTs–LiOH was considerably enhanced, facilitating an easier and more rapid reaction of H_2O and LiOH than before.

Fig. 6d presented the *in situ* DRIFT spectroscopy of dehydration reaction of Ni-CNTs–$LiOH \cdot H_2O$. When Ni-CNTs–$LiOH \cdot H_2O$ was heated to 50 °C, the peak intensities of OH in structural H_2O (3679 cm^{-1} and 1573 cm^{-1}) started to decrease; beyond 60 °C, $LiOH \cdot H_2O$ was continuously dehydrated until the structure of H_2O was fully lost. Meanwhile, the peaks of OH (3181 cm^{-1} and 1625 cm^{-1}) in physical adsorbed H_2O appeared, increased from 50 °C to 90 °C, and eventually decreased; this trend was ascribed to the easy removal of H_2O at elevated temperature. The formed water could also produce hydrogen bonding with C=O groups (1720 cm^{-1}) on the surface of Ni-CNTs, thereby causing a shift of the C=O band to a lower position (1710 cm^{-1}). During the dehydration reaction from 30 °C to 120 °C, the intensities of C=O and C–OH (3520 cm^{-1} and 1400 cm^{-1}) peaks showed no obviously change, indicating

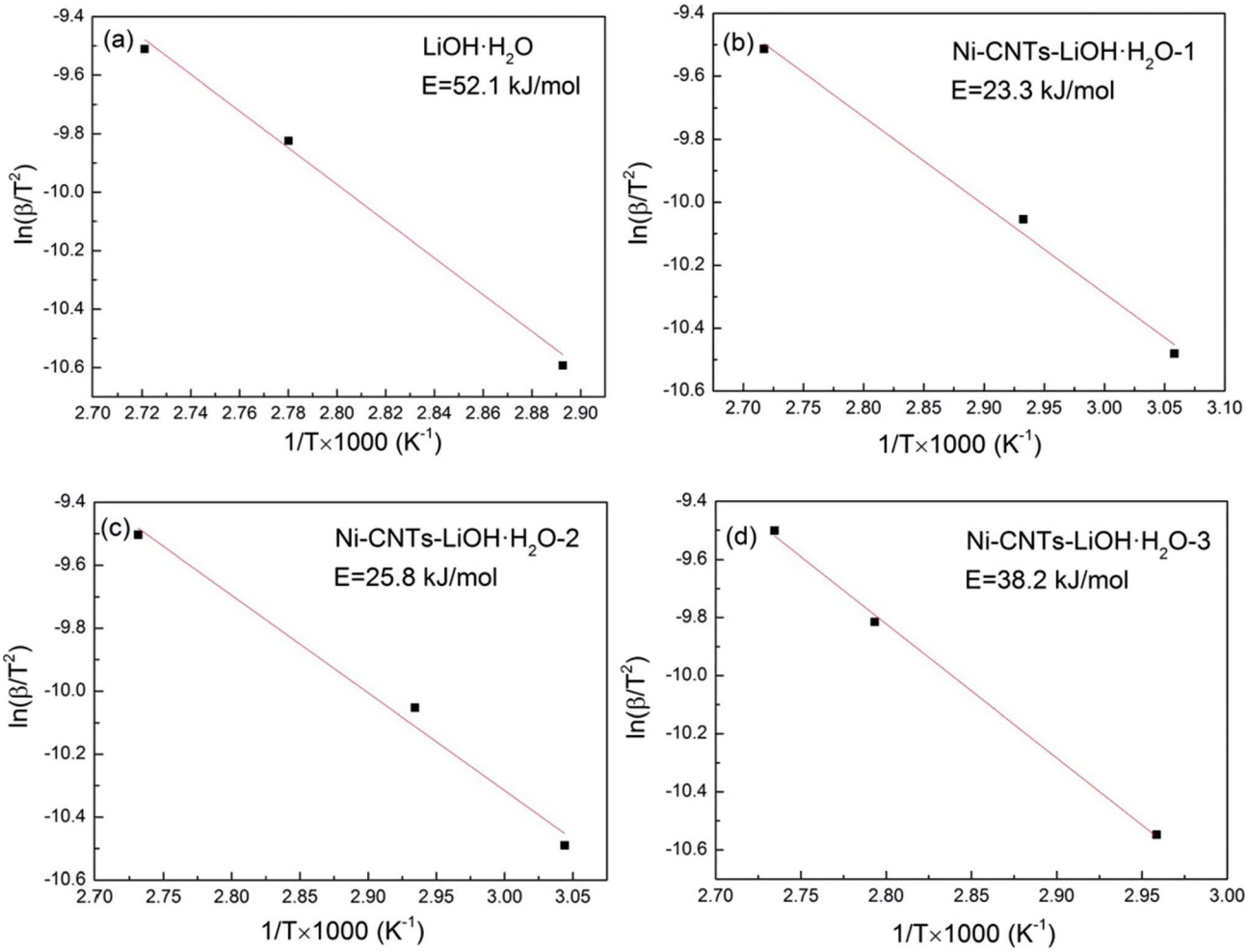

Fig. 7 The activation energy of dehydration reaction of (a) $LiOH \cdot H_2O$, (b) Ni-CNTs–$LiOH \cdot H_2O$-1, (c) Ni-CNTs–$LiOH \cdot H_2O$-2, (d) Ni-CNTs–$LiOH \cdot H_2O$-3.

that the physical–chemical property of Ni-CNTs is steady within the total dehydration temperature range. The dehydration temperature of Ni-CNTs–$LiOH \cdot H_2O$ was approximately 10 °C lower than that of pure $LiOH \cdot H_2O$; this finding is in good agreement with the results of the TG-DSC test.

As shown in Fig. 7, the activation energies of the dehydration reaction of (a) $LiOH \cdot H_2O$, (b) Ni-CNTs–$LiOH \cdot H_2O$-1, (c) Ni-CNTs–$LiOH \cdot H_2O$-2, and (d) Ni-CNTs–$LiOH \cdot H_2O$-3 as obtained using the Ozawa method are 52.1, 23.3, 25.8, and 38.2 kJ mol^{-1}, respectively.[36] The activation energies of composite TCMs were markedly lower than that of pure $LiOH \cdot H_2O$ due to the surface effect of nano-$LiOH \cdot H_2O$ composite TCMs. The specific surface area or surface-to-volume ratio, which changes with particle size, depends on activation energy.[47] By combining the SEM, TEM, and BET characterization results, it could be found that as the Ni-CNT content increased, the specific surface area of the composite TCMs also increased, whereas the particle size of $LiOH \cdot H_2O$ decreased. The activation energy of $LiOH \cdot H_2O$ dehydration reaction in composite TCMs showed similar trend to the particle size variation of $LiOH \cdot H_2O$. This trend can be attributed to diminished particle size, leading to increased surface-to-volume ratio and molar surface energy of nanoparticles, which mainly result in decreased activation energy.[48,49] In summary, the addition of 3D-carbon nanomaterial Ni-CNTs can not only enhance water absorption at the LiOH particle surface but also decrease activation energy. Owing to the addition of Ni-CNTs, $LiOH \cdot H_2O$ are dehydrated more easily, and the reaction mechanism of composited TCMs may deviate from that of pure $LiOH \cdot H_2O$ because of the surface effect of 3D Ni-CNTs–$LiOH \cdot H_2O$ nanocomposite materials during the thermochemical reaction process.

4. Conclusions

For investigating the effects of *in situ* formed 3D-carbon nanoadditives (Ni-CNTs) on the thermal performance of low-temperature $LiOH \cdot H_2O$-based composites as thermochemical heat storage materials, four kinds of $LiOH \cdot H_2O$-based composite TCMs were successfully constructed and characterized. Owing to the addition of 3D-carbon nanoadditives, the nanoscale (5–15 nm) $LiOH \cdot H_2O$ particles were well dispersed in the composite with Ni-CNTs. The heat storage capacity and thermal conductivity of the composite materials were markedly improved. Meanwhile, the hydration rate was enhanced due to

the hydrogen bonding formed between H_2O and hydrophilic groups on the surface of Ni-CNTs, as shown by the combined results of *in situ* DRIFT spectroscopy characterization and the heat storage performance test. The activation energy for the thermochemical reaction process notably decreased after the addition of Ni-CNTs possibly because Ni-CNTs provide efficient hydrophilic reaction interface and exhibit surface effect in the hydration reaction. Among these TCMs, Ni-CNTs–$LiOH \cdot H_2O$-1 showed the lowest activation energy (23.3 kJ mol^{-1}), highest thermal conductivity (3.78 W m^{-1} K^{-1}), and highest heat storage density (3935 kJ kg^{-1}), which is 5.9 times higher than pure lithium hydroxide after the same hydration duration. The heat storage density and the thermal conductivity of Ni-CNTs–$LiOH \cdot H_2O$ are great higher than 1D MWCNTs and 2D graphene oxide modified $LiOH \cdot H_2O$. The selection of 3D carbon nano-additives as composed part of the chemical heat storage materials is a very efficient way to enhance comprehensive performance of heat storage activity component.

Conflicts of interest

There are no conflicts to declare.

Acknowledgements

This work was supported by Science and Technology Planning Project of Guangdong Province, China (2016A050502040), Research project of the Chinese Academy of Sciences (QYZDY-SSW-JSC038) and the National Natural Science Foundation of China (No. 51406209).

References

1 A. Gil, M. Medrano, I. Martorell, A. Lázaro, P. Dolado, B. Zalba and L. F. Cabeza, State of the art on high temperature thermal energy storage for power generation. Part 1-concepts, materials and modellization, *Renewable Sustainable Energy Rev.*, 2010, **14**, 31–55.

2 Q. Q. Tang, J. Sun, S. M. Yu and G. C. Wang, Improving thermal conductivity and decreasing supercooling of paraffin phase change materials by n-octadecylamine-functionalized multi-walled carbon nanotubes, *RSC Adv.*, 2014, **4**, 36584–36590.

3 V. A. Salomoni, C. E. Majorana, G. M. Giannuzzi, A. Miliozzi, R. D. Maggio, F. Girardi, D. Mele and M. Lucentini, Thermal storage of sensible heat using concrete modules in solar power plants, *Sol. Energy*, 2014, **103**, 303–315.

4 L. Miró, M. E. Navarro, P. Suresh, A. Gil, A. I. Fernández and L. F. Cabeza, Experimental characterization of a solid industrial by-product as material for high temperature sensible thermal energy storage (TES), *Appl. Energy*, 2014, **113**, 1261–1268.

5 Z. Y. Lu, D. S. Hou, B. W. Xu and Z. J. Li, Preparation and characterization of an expanded perlite/paraffin/graphene oxide composite with enhanced thermal conductivity and leakage-bearing properties, *RSC Adv.*, 2015, **5**, 107514–107521.

6 A. Kardam, S. S. Narayanan, N. Bhardwaj, D. Madhwal, P. Shukla, A. Verma and V. K. Jain, Ultrafast thermal charging of inorganic nano-phase change material composites for solar thermal energy storage, *RSC Adv.*, 2015, **5**, 56541–56548.

7 A. Shkatulov and Y. Aristov, Calcium hydroxide doped by KNO_3 as a promising candidate for thermochemical storage of solar heat, *RSC Adv.*, 2017, **7**, 42929–42939.

8 M. Rothensteiner, A. Bonk, U. F. Vogt, H. Emeriche and J. A. V. Bokhoven, Structural changes in equimolar ceria–hafnia materials under solar thermochemical looping conditions: cation ordering, formation and stability of the pyrochlore structure, *RSC Adv.*, 2017, **7**, 53797–53809.

9 T. Yan, R. Z. Wang, T. X. Li, L. W. Wang and I. T. Fred, A review of promising candidate reactions for chemical heat storage, *Renewable Sustainable Energy Rev.*, 2015, **43**, 13–31.

10 P. Pardo, A. Deydier, Z. Anxionnaz-Minvielle, S. Rougé, M. Cabassud and P. Cognet, A review on high temperature thermochemical heat energy storage, *Renewable Sustainable Energy Rev.*, 2014, **32**, 591–610.

11 H. Ishitobi, K. Uruma, M. Takeuchi, J. Ryu and Y. Kato, Dehydration and hydration behavior of metal-salt-modified materials for chemical heat pumps, *Appl. Therm. Eng.*, 2013, **50**, 1639–1644.

12 H. Ogura, T. Yamamoto and H. Kage, Efficiencies of CaO/H_2O/$Ca(OH)_2$ chemical heat pump for heat storing and heating/cooling, *Energy*, 2003, **28**, 1479–1493.

13 D. A. Sheppard, M. Paskevicius and C. E. Buckley, Thermodynamics of hydrogen desorption from $NaMgH_3$ and its application as a solar heat storage medium, *Chem. Mater.*, 2011, **23**, 4298–4300.

14 K. Kyaw, T. Shibata, F. Watanabe, H. Matsuda and M. Hasatani, Applicability of zeolite for CO_2 storage in a CaO-CO_2 high temperature energy storage system, *Energy Convers. Manage.*, 1997, **38**, 1025–1033.

15 X. X. Yang, H. Y. Huang, Z. H. Wang, M. Kubota, Z. H. He and N. Kobayashi, Facile synthesis of graphene oxide-modified lithium hydroxide for low-temperature chemical heat storage, *Chem. Phys. Lett.*, 2016, **644**, 31–34.

16 W. Wongsuwan, S. Kumar, P. Neveu and F. Meunier, A review of chemical heat pump technology and applications, *Appl. Therm. Eng.*, 2001, **21**, 1489–1519.

17 M. Kubota, N. Horie, H. Togari and H. Matsuda, Improvement of hydration rate of LiOH/$LiOH \cdot H_2O$ reaction for low-temperature thermal energy storage, *Annual Meeting of Japan Society of Refrigerating and Air Conditioning Engineers*, Tokai University, Japan, 2013.

18 G. Whiting, D. Grondin, S. Bennici and A. Auroux, Heats of water sorption studies on zeolite-$MgSO_4$ composites as potential thermochemical heat storage materials, *Sol. Energy Mater. Sol. Cells*, 2013, **112**, 112–119.

19 S. Hongois, F. Kuznik, P. Stevens and J. J. Roux, Development and characterisation of a new $MgSO_4$-zeolite composite for long-term thermal energy storage, *Sol. Energy Mater. Sol. Cells*, 2011, **95**, 1831–1837.

20 Z. P. Zeng, X. C. Gui, Z. Q. Lin, L. H. Zhang, J. Yi, A. Y. Cao, Y. Zhu, R. Xiang, T. Z. Wu and Z. K. Tang, Carbon nanotube

sponge-array tandem composites with extended energy absorption range, *Adv. Mater.*, 2013, **25**, 1185–1191.

21 K. Zhang, T. T. Li, L. Ling, H. F. Lu, L. Tang, C. W. Li, L. J. Wang and Y. G. Yao, Facile synthesis of high density carbon nanotube array by a deposition-growth-densification process, *Carbon*, 2017, **114**, 435–440.

22 E. Muñoz-Sandoval, A. J. Cortes-Lopez, B. Flores-Gomez, J. L. Fajardo-Díaz, R. Sanchez-Salas and F. Lopez-Urías, Carbon sponge-type nanostructures based on coaxial nitrogen-doped multiwalled carbon nanotubes grown by CVD using benzylamine as precursor, *Carbon*, 2017, **115**, 409–421.

23 J. K. Chen, X. C. Gui, Z. Q. Lin, Z. K. Tang, M. M. Lee, A. Wokaun and T. Lippert, Pulsed ultra-violet laser interactions with ultra-low-density porous carbon nanotube sponges, *Carbon*, 2015, **93**, 604–610.

24 X. Su, J. Wu and B. J. Hinds, Catalytic activity of ultrathin Pt films on aligned carbon nanotube arrays, *Carbon*, 2011, **49**(4), 1145–1150.

25 Y. Shen, D. Sun, L. Yu, W. Zhang, Y. Y. Shang, H. R. Tang, J. F. Wu, A. Y. Cao and Y. H. Huang, A high-capacity lithium-air battery with Pd modified carbon nanotube sponge cathode working in regular air, *Carbon*, 2013, **62**, 288–295.

26 Q. Cao, S. J. Han, G. S. Tulevski, Y. Zhu, D. D. Lu and W. Haensch, Arrays of single-walled carbon nanotubes with full surface coverage for high-performance electronics, *Nat. Nanotechnol.*, 2013, **8**, 180–186.

27 L. M. Zhang, X. L. Sui, L. Zhao, G. S. Huang, D. M. Gu and Z. B. Wang, Three-dimensional hybrid aerogels built from graphene and polypyrrole-derived nitrogen-doped carbon nanotubes as a high-efficiency Pt-based catalyst support, *Carbon*, 2017, **121**, 518–526.

28 B. W. Xu and Z. J. Li, Paraffin/diatomite/multi-wall carbon nanotubes composite phase change material tailor-made for thermal energy storage cement-based composites, *Energy*, 2014, **72**, 371–380.

29 W. D. Liang, Y. Wu, H. X. Sun, Z. Q. Zhu, P. S. Chen, B. P. Yang and A. Li, Halloysite clay nanotubes based phase change material composites with excellent thermal stability for energy saving and storage, *RSC Adv.*, 2016, **6**, 19669–19675.

30 Z. P. Liu, R. Q. Zou, Z. Q. Lin, X. C. Gui, R. J. Chen, J. H. Lin, Y. Y. Shang and A. Y. Cao, Tailoring carbon nanotube density for modulating electro-to-heat conversion in phase change composites, *Nano Lett.*, 2013, **13**(9), 4028–4035.

31 X. X. Yang, S. J. Li, H. Y. Huang, J. Li, N. Kobayashi and M. Kubota, Effect of carbon nanoadditives on lithium hydroxide monohydrate-based composite materials for low temperature chemical heat storage, *Energies*, 2017, **10**(5), 644–653.

32 S. J. Li, H. Y. Huang, X. X. Yang, C. G. Wang, N. Kobayashi and M. Kubota, A facile method to construct graphene oxide-based magnesium hydroxide for chemical heat storage, *Nanoscale Microscale Thermophys. Eng.*, 2017, **21**(1), 1–7.

33 S. J. Li, H. Y. Huang, X. X. Yang, Y. Bai, J. Li, N. Kobayashi and M. Kubota, Hydrophilic substance assisted low temperature $LiOH \cdot H_2O$ based composite thermochemical materials for thermal energy storage, *Appl. Therm. Eng.*, 2018, **128**, 706–711.

34 O. Myagmarjav, J. Ryu and Y. Kato, Lithium bromide-mediated reaction performance enhancement of a chemical heat-storage material for magnesium oxide/water chemical heat pumps, *Appl. Therm. Eng.*, 2014, **63**, 170–176.

35 J. K. Chinthaginjala, D. B. Thakur, K. Seshan and L. Lefferts, How carbon-nano-fibers attach to Ni foam, *Carbon*, 2008, **46**, 1638–1647.

36 M. Kubota, S. Matsumoto, H. Matsuda, H. Y. Huang, Z. H He and X. X. Yang, Chemical heat storage with $LiOH/LiOH \cdot H_2O$ reaction for low-temperature heat below 373 K, *Adv. Mater. Res.*, 2014, **953–954**, 757–760.

37 D. S. Yuan, J. X. Chen, J. H. Zeng and S. X. Tan, Preparation of monodisperse carbon nanospheres for electrochemical capacitors, *Electrochem. Commun.*, 2008, **10**, 1067–1070.

38 M. Mehrali, L. S. Tahan, M. Mehrali, T. M. I. Mahlia and H. S. Cornelis Metselaar, Effect of carbon nanospheres on shape stabilization and thermal behavior of phase change materials for thermal energy storage, *Energy Convers. Manage.*, 2014, **88**, 206–213.

39 X. C. Liu, Y. Osaka, H. Y. Huang, H. Huhetaoli, J. Li, X. X. Yang, S. J. Li and N. Kobayashi, Development of low-temperature desulfurization performance of a MnO_2/AC composite for a combined SO_2 trap for diesel exhaust, *RSC Adv.*, 2016, **6**, 96367–96375.

40 J. F. Wang, H. Q. Xie, Z. Xin, Y. Li and L. F. Chen, Enhancing thermal conductivity of palmitic acid based phase change materials with carbon nanotubes as fillers, *Sol. Energy*, 2010, **84**, 339–344.

41 G. Q. Zhang, Z. Li, H. Y. Zheng, T. J. Fu, Y. B. Ju and Y. C. Wang, Influence of the surface oxygenated groups of activated carbon on preparation of a nano Cu/AC catalyst and heterogeneous catalysis in the oxidative carbonylation of methanol, *Appl. Catal., B*, 2015, **179**, 95–105.

42 B. X. Wang, L. P. Zhou and X. F. Peng, Surface and size effects on the specific heat capacity of nanoparticles, *Int. J. Thermophys.*, 2005, **27**, 139–151.

43 L. J. Chen, R. Q. Zou, W. Xia, Z. P. Liu, Y. Y. Shang, J. L. Zhu, Y. X. Wang, J. H. Lin, D. G. Xia and A. Y. Cao, Electro-and photodriven phase change composites based on wax-infiltrated carbon nanotube sponges, *ACS Nano*, 2012, **6**, 10884–10892.

44 T. Szabo, O. Berkesi, P. Forgo, K. Josepovits, Y. Sanakis, D. Petridis and I. Dekany, Evolution of surface functional groups in a series of progressively oxidized graphite oxides, *Chem. Mater.*, 2006, **18**, 2740–2749.

45 S. F. Weng and Y. Z. Xu, *Fourier transform infrared spectrum analysis*, Chemical Industry Press of China, 2016.

46 L. Zhao, X. Y. Li, C. Hao and C. L. Raston, SO_2 adsorption and transformation on calcined NiAl hydrotalcite-like compounds surfaces: an in situ FTIR and DFT study, *Appl. Catal., B*, 2012, **117–118**, 339–345.

47 K. Hoang, A. Janotti and C. G. Van de Walle, The particle-size dependence of the activation energy for decomposition of lithium amide, *Angew. Chem.*, 2011, **123**, 10352–10355.
48 Z. X. Cui, Y. Q. Xue, L. B. Xiao and T. T. Wang, Effect of particle size on activation energy for thermal decomposition of nano-$CaCO_3$, *J. Comput. Theor. Nanosci.*, 2013, **10**, 569–572.
49 Z. Y. Li, K. Yu, J. Liu, Y. W. Tian and Y. C. Zhai, Effect of diameter on apparent activation energy of non-isothermal decomposition reaction of nano-$Mg(OH)_2$ powder, *Curr. Nanosci.*, 2012, **8**, 97–101.